

Microwave Imaging for Medical Diagnosis

George G. Cheng¹, Yong Zhu², and Jan Grzesik³

Allwave Corporation, 3860 Del Amo Blvd., #404, Torrance, CA 90503, USA
¹george@allwavecorp.com, ²yong@allwavecorp.com, ³jan@allwavecorp.com

Abstract

We introduce an efficient microwave imaging technique for medical applications, especially suited for breast cancer detection. The imaging system consists of a fixed source for transmit on one end, and a planar array of receiving sensors on the other, with the target placed in between. The image of the internal organ tissue under examination is thus obtained across a three-dimensional region, based upon the data collected by these sensors, using our field mapping algorithm (FMA).

An image of tissue structure can be obtained through application of the FMA. This algorithm transforms electromagnetic fields upon one surface to another in an exact sense. It determines the entire electric and magnetic field everywhere based on two tangential field components, either electric or magnetic, on a surface, be it a plane, a sphere, or a cylinder. The geometry of the biological organs is then ascertained from the field polarization attributes, which indicate tissue structure. In particular, the tissue mass associated with any given field distribution can thus be revealed as to its structure and electrical properties by way of the field polarization attributes.

Moreover, inasmuch as our FMA provides interior fields on the basis of surface measurements, performed at some remove from actual *in vivo* material, we hold in our hands a rapid, simple, and fully non-destructive method for providing tissue structure across entire organ volumes, without any significant spatial restriction or fear of tissue damage due to biological intrusion.

Six test cases, including analytic examples, FDTD simulation runs, and hardware measurements, are given for verification, with most promising results evident throughout.

1 Introduction

Imaging techniques can in general be categorized as inverse source and inverse medium problems. The former includes holography, ISAR, remote sensing, etc., and, among the latter, computer-aided tomography is perhaps the most familiar. We propose a new concept which solves both inverse source and inverse medium problems in the same fashion. In other words, one and the same theory, one and the same set of formulae are applied to both source and medium inversion.

2 Theory

The field mapping is an algorithm which transforms electromagnetic fields from one surface to another in an exact sense. This algorithm determines the entire electric and magnetic field everywhere based on two tangential field components, either electric or magnetic, on a surface, say a plane, a sphere, or a cylinder. This algorithm takes the form $\mathbf{E}(\mathbf{r}) = \mathbf{T}(\mathbf{r}, \mathbf{r}_s) [\mathbf{E}^t(\mathbf{r}_s)]$, where \mathbf{r} is any point vector in space, \mathbf{r}_s a point vector on the data surface, $\mathbf{E}(\mathbf{r})$ the electric field at any \mathbf{r} , $\mathbf{E}^t(\mathbf{r}_s)$ the tangential electric field at \mathbf{r}_s , while $\mathbf{T}(\mathbf{r}, \mathbf{r}_s)$, called the “*Mapping Kernel*,” transforms fields from one surface $S(\mathbf{r}_s)$ to another $S(\mathbf{r})$. In particular, the medium associated with the field distribution $\mathbf{E}(\mathbf{r})$ can thus be revealed as to its structure and electrical properties by way of the field polarization attributes. The field mapping is applicable in any region, either interior or exterior to the data surface, or in between. The field mapping algorithm is a direct, closed-form solution which is numerically straightforward and efficient.

The imaging procedure consists of two steps. First, one obtains the electric field in the vicinity of the region of interest. Normally the data is collected on a planar, spherical, or cylindrical surface. Regardless of the source, the required field can be of either a transmitted or reflected kind. Second, this near-field data is utilized as input to the imaging algorithm, whose output reveals the medium structure across the region under investigation.

3 Implementation

The imaging algorithm has been implemented and verified for various medium environments, with its input data generated through analytic solutions (Cases 1-3), software simulation (Case 4), and hardware measurement (Cases 5-6). All six test cases are presented here by way of verification. In particular, the hardware tests are focused specifically on biological tissue.

3.1 Analytic Examples

Three examples for imaging based on analytic near-field data over planar, spherical and cylindrical surfaces respectively are given in Cases 1-3 to demonstrate our FMA method of solving inverse source problems.

Case 1: Planar Surface: Circular Aperture Source

Case 1 involves a circular aperture in an infinite conducting plane as shown in Fig.1a. Its planar near-field data at $z = 30\lambda$, obtained analytically, also appears on the right in Fig.1a. The imaging achieved by “Field Mapping” the near-field data from the plane at $z = 30\lambda$ to the plane at $z = 0$, is shown in Fig.1b, where the circular aperture is clearly visible. Also apparent is the excellent agreement between the analytic and calculated fields on the XZ symmetry mid-plane at $y=0$.

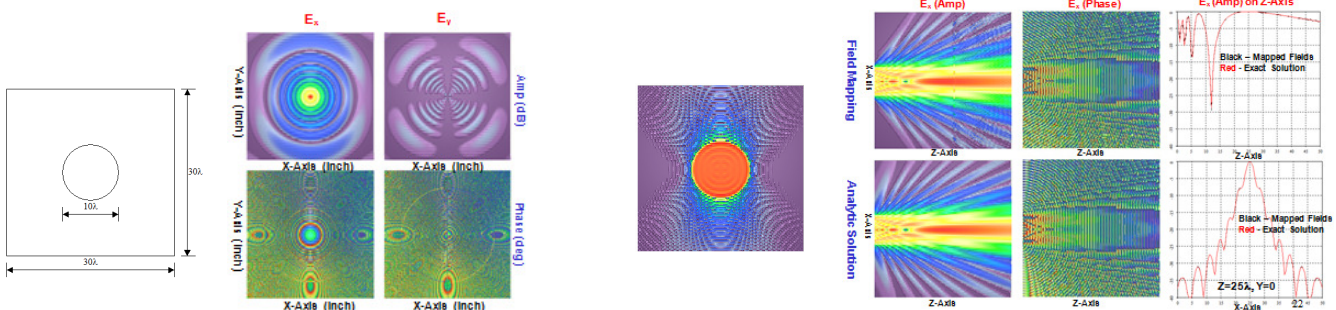


Fig.1a A circular aperture and its near-field at $z=30\lambda$ Fig.1b Output: *Left*, XY plane at $z=0$, *right*, fields on $50\lambda \times 50\lambda$ XZ plane at $y=0$

Case 2: Spherical Surface: A Slotted Conducting Sphere

Case 2 entails a slotted conducting sphere of radius a excited by E_θ across an infinitesimal gap located at $\theta = \theta_0$ as shown in Fig.2a. The tangential electric field on an outer sphere $r > a$ can be obtained analytically for use as input data to the imaging algorithm. In the present case, $a = 5\lambda$, $\theta_0 = 40^\circ$, $r = 10\lambda$. The input data in Fig.2b is the electric field on an $r = 10\lambda$ spherical surface, and the output of the imaging algorithm is shown in Fig.2c, where both the excited slot astride a null tangential field across the remainder of the sphere are plainly evident.

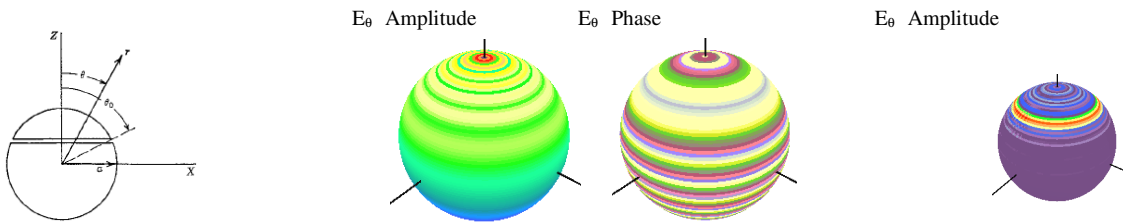


Fig.2a Slotted conducting sphere, $a=5\lambda$, $\theta_0=40^\circ$ Fig.2b Input: E_θ on spherical surface at $r=10\lambda$ Fig.2c Output: E_θ on sphere at $r=5\lambda$

Case 3: Cylindrical Surface: Three Dipoles

Case 3 features three dipoles in space. Their layout and near-field data on a cylindrical surface at $\rho = 40''$ are shown in Fig.3a, and the imaging results in Fig.3b, respectively. The calculated images are shown on two cylindrical surfaces: (a) $\rho = 10''$, the two hot spots at $(\rho, \phi, z) = (10'', 0^\circ, 15'')$, $(10'', 90^\circ, -10'')$ identify two of the three dipole locations; and (b) $\rho = 5''$, the hot spot at $(\rho, \phi, z) = (5'', 180^\circ, 5'')$ is exactly where the third dipole is located. As expected all three dipoles are well resolved.

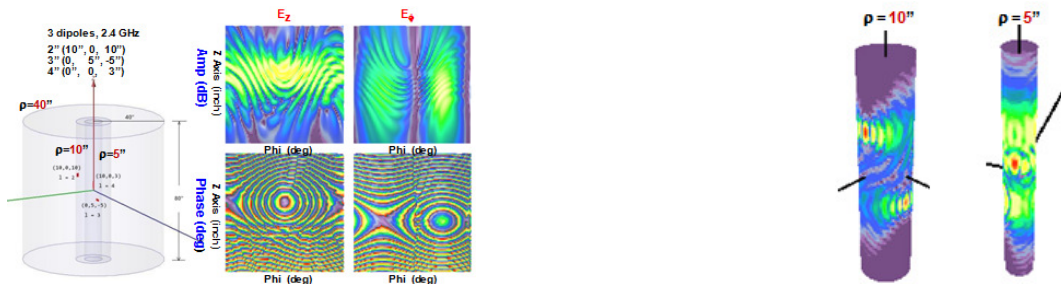


Fig.3a Three dipoles, and their 2.4 GHz near-field on cylindrical surface at $\rho=40''$, $Z=160''$ Fig.3b Output: Fields in the source regions

3.2 Software Simulations

Case 4 is an example in which the input data were generated through FDTD software simulation. As opposed to source inversion in Cases 1-3, we offer Case 4 as an example of solving inverse medium problems.

Case 4: A Slotted Array Antenna

Case 4 involves a 12" diameter X-band slotted array antenna as in Fig. 4a. The input data in Fig. 4b is the computed electric field from a commercial FDTD software package. The output of the field mapping algorithm is shown in Fig. 4c. Excellent agreement between the field mapping and FDTD simulation outcomes is clearly visible.

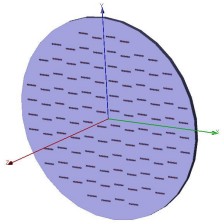


Fig.4a X-band slotted array antenna

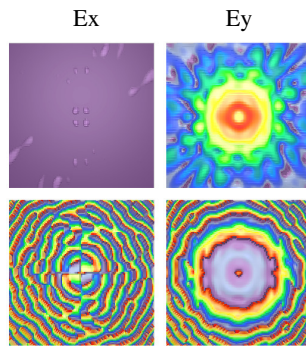


Fig.4b FDTD simulated fields on 28"x28" XY plane at $z=12"$, 9.2 Ghz

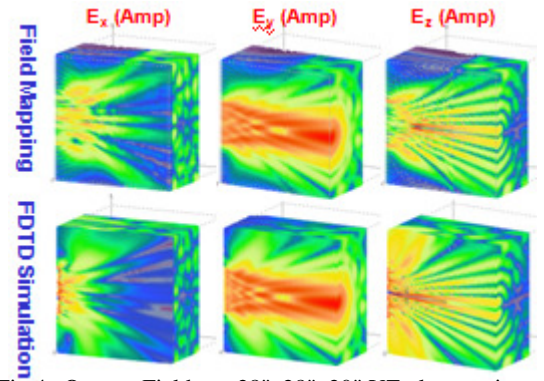


Fig.4c Output: Fields on 28"x28"x20" YZ plane region

3.3 Hardware Measurement

The final test cases, 5 and 6, build upon outright hardware measurements in which the inputs to the imaging algorithm are the raw near-field data. They represent, moreover, a direct verification of medium inversion as gotten under the guidance of our FMA. The required input data is simply a single near-field measurement on a single surface, at a single frequency, and the processing time is normally on the order of a few minutes in real time. Once the data is taken, the imaging of the medium can be obtained in just few minutes of FMA processing, because the FMA inherently embodies a direct field inversion. In Case 5 we consider dielectric material with metallic inclusions, whereas in Case 6 we report tests on two biological tissue samples particularly intended to demonstrate FMA use in medical applications.

Case 5: A 4-Layer Material

Case 5 presents FMA imaging for a four-layer material, in which several metallic items are sandwiched between dielectric sheets. The measurement setup is shown in Fig. 5a, wherein the transmit source is a y-polarized horn antenna on the left, while reception occurs via a waveguide probe on the right. The input data to the imaging algorithm is the measured electric field, both E_x and E_y components, on a 24" x 24" XY-plane 5" beyond the material, as shown in Fig. 5b. The output results are the medium imaging in twelve cross sections cutting through the material, indicated in Fig. 5c. The images are revealed by the dominant field polarization attribute, E_y in this case, over twelve planes under examination as shown in Fig. 5d. It is observed that the metallic objects are clearly indicated on all five faces 2, 4, 6, 8, and 10 of the layered material.

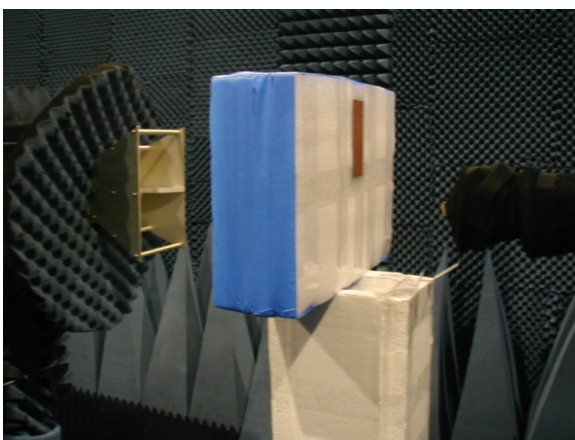


Fig.5a Measurement setup of the 4-layer material

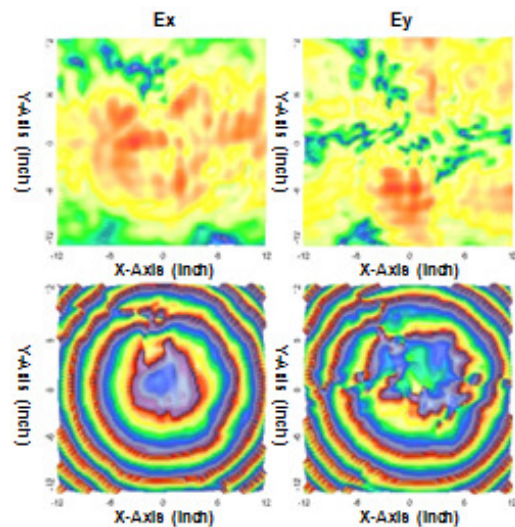


Fig. 5b Measured near-field data on 24"x24" XY plane at $Z=5"$, 9.2 GHz

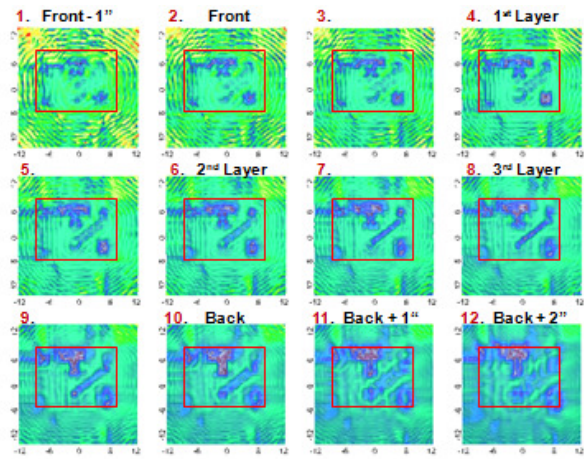
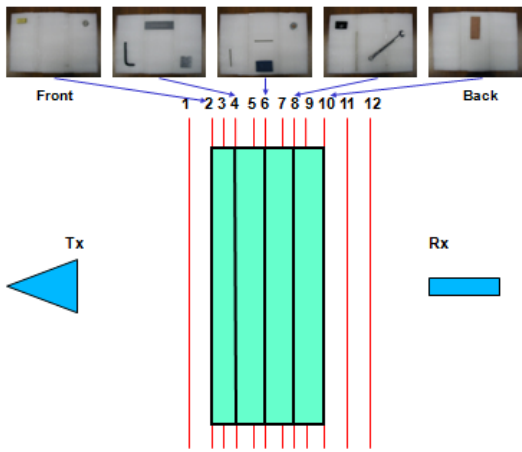


Fig.5c 12 planes cutting through 4-layer material are under investigation Fig. 5d Output: Ey field distributions on the 12 specified planes

Case 6: Biological Tissues

The goal for Case 6 is to determine the structure of biological tissue from the electromagnetic waves that have penetrated across it. Two types of pork meat were tested in this case, one with a structural bone (Fig. 6d), and the other without (Fig. 6a). We used an X-band slotted array antenna as a transmit source, with the pork meat placed in the middle, and received by a probe 6" (away from meat) downstream scanning in a raster fashion as shown in Fig. 6a. The near-field was taken across a 16"x16" XY-plane in Fig. 6b, and the output of the FMA, based upon this near-field data, showed the Ey distribution from Fig. 6c over the middle cross section (XY-plane) of the meat. It can be seen that the field distribution resembles the soft, boneless tissue structure. In similar fashion, Fig. 6d conveys the test setup for a pork sample with bone included, Fig. 6e is the measured near-field data supplying an input to our FMA, with the field distribution over the middle cross section (XY-plane) of the pork shown as FMA output in Fig. 6f. Bone presence is clearly evident from the results.



Fig. 6a Pork meat I, without bone

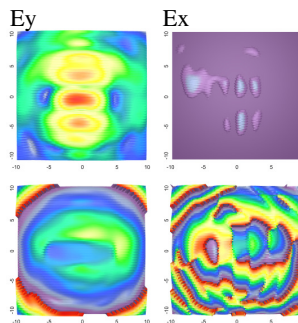


Fig. 6b Measured near-field data of pork I on 16"x16" XY-plane at Z=6"(away from meat), at 9.2 GHz

Ey @ cross-section 2" inside meat

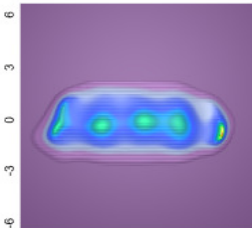


Fig. 6c Output: Ey on 8"x8" XY-plane at Z=8"



Fig. 6d Pork meat II, with bone

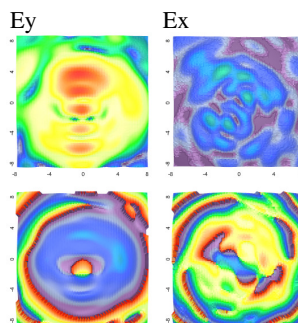


Fig. 6e Measured near-field data of pork II on 16"x16" XY-plane at Z=6"(away from meat), at 9.2 GHz

Ey @ cross-section 1" inside meat

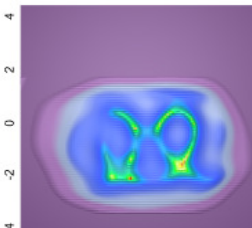


Fig. 6f Output: Ey on 8"x8" XY-plane at Z=7"

4 Conclusion

We have implemented and verified in six test cases our imaging algorithm based on the field mapping technique: three analytic examples involving a circular aperture, a metallic sphere with radiating gap, and a triplet of dipoles; one FDTD example of an X-band slotted array antenna; plus two hardware measurements, one of which is intended to detect hard metallic enclosures, and two biological tissue samples, with and without bone. Excellent results were obtained in all six situations. The FMA imaging algorithm is so efficient that it may be used for a variety of medical applications, particularly for breast cancer detection, on behalf of which an in-depth investigation of our own is currently underway.